

# Theoretical Investigation of Performance-Improved Ferroelectric Tunnel Junction Based on Trap-Assisted Tunneling

Shi-Xi Kong<sup>1, a)</sup> and Tuo-Hung Hou<sup>1, 2, b)</sup>

<sup>1)</sup>Department of Electronics and Electrical Engineering, National Yang Ming Chiao Tung University, 30010, Hsinchu, Taiwan, Republic of China

<sup>2)</sup>Institute of Electronics, National Yang Ming Chiao Tung University, Hsinchu, 30010, Taiwan, Republic of China

CMOS-compatible HfO<sub>2</sub>-based ferroelectric tunnel junction (FTJ) has attracted significant attention as a promising candidate for in-memory computing (IMC) due to its extremely low power consumption. However, conventional FTJs face inherent challenges and hinder their practical applications. Insufficient current density ( $J_{\text{ON}}$ ) and limited on-off current ratios in FTJs are primarily constrained by their dependence on direct tunneling (DT) and Fowler-Nordheim (FN) tunneling mechanisms. Building on previous experimental results, this paper proposes a trap-assisted tunneling (TAT)-based FTJ that leverages the TAT mechanism to overcome these limitations. A comprehensive FTJ model integrating ferroelectric (FE) switching, DT, FN tunneling, and TAT mechanisms is developed, enabling detailed analyses of the trap conditions and their impact on performance. Through systematic optimization of trap parameters and device structure, the TAT-based FTJ achieves ultra-high  $J_{\text{ON}}$  and a remarkable on-off current ratio, meeting the nanoscale IMC requirements. The results highlight the potential of TAT-based FTJs as high-performance memory solutions for IMC applications.

Ferroelectric tunnel junction (FTJ) is a non-volatile memory (NVM) that allows non-destructive readout between opposite ferroelectric polarization ( $P_{\text{FE}}$ ) states through the tunnel electroresistance (TER) effect.<sup>1,2</sup> Due to its extremely low power consumption, CMOS-compatible HfO<sub>2</sub>-based FTJ has gained significant attention as a promising candidate for in-memory computing (IMC).<sup>3-5</sup> To balance the power and the latency, a desirable memory cell for IMC requires on-state resistance ( $R_{\text{ON}}$ ) in the range of 100 k $\Omega$  ~ 1 M $\Omega$ .<sup>6,7</sup> As the device area is scaled down to nanoscale, such as a 10 nm  $\times$  10 nm FTJ cell and a read voltage of 0.1 V, achieving an ultra-high on-current density ( $J_{\text{ON}}$ ) exceeding 10<sup>5</sup> A/cm<sup>2</sup> becomes imperative. Additionally, a high on-off current ratio ( $J_{\text{ON}}/J_{\text{OFF}}$ ) and low-voltage operation are crucial to enabling high-performance IMC.<sup>6,7</sup>

To date, conventional FTJs have predominantly relied on direct tunneling (DT) and Fowler-Nordheim (FN) tunneling mechanisms, as shown in Fig. 1(a).<sup>8</sup> However, these mechanisms face critical limitations in IMC applications. First, the  $J_{\text{ON}}$  falls far below the required 10<sup>5</sup> A/cm<sup>2</sup>, even with aggressive thickness scaling down to the ultra-thin range (1–3 nm), achieving  $J_{\text{ON}}$  above 10<sup>2</sup> A/cm<sup>2</sup> remains elusive.<sup>9-11</sup> Second, while incorporating dielectric materials such as SiO<sub>2</sub> or Al<sub>2</sub>O<sub>3</sub> as an interfacial layer (IL) has been explored to enhance the  $J_{\text{ON}}/J_{\text{OFF}}$  ratio, exceeding a ratio of 100 $\times$  remains a considerable challenge.<sup>12,13</sup> Moreover, attempts to improve either  $J_{\text{ON}}$  or the  $J_{\text{ON}}/J_{\text{OFF}}$  ratio often result in inherent trade-offs, limiting the performance of conventional FTJs.<sup>2</sup> Interestingly, Chu et al. experimentally reported that a 3 nm-thick HZO FTJ with an addi-

tional 1.5 nm-thick top IL (TIL) demonstrated simultaneous increases in both  $J_{\text{ON}}$  and  $J_{\text{ON}}/J_{\text{OFF}}$ , as shown in Fig. 1(b).<sup>11</sup> This unexpected enhancement in  $J_{\text{ON}}$  with a thicker TIL cannot be explained by DT and FN tunneling mechanisms alone and was attributed to traps introduced by the Al<sub>2</sub>O<sub>3</sub> layer. However, conflicting reports in the literature often identify traps as sources of leakage currents.<sup>14,15</sup> Therefore, understanding the mechanism enabling simultaneous enhancement of  $J_{\text{ON}}$  and  $J_{\text{ON}}/J_{\text{OFF}}$  is essential to overcoming the limitations of conventional FTJs and advancing their application in IMC.

In this work, a novel TAT-based FTJ, where the trap-assisted tunneling (TAT)<sup>16,17</sup> serves as the dominant tunneling mechanism, is proposed and investigated, as shown in Fig. 1(a). To perform a comprehensive theoretical investigation of TAT-based FTJ, an improved FTJ model was developed, integrating FE switching, DT, FN tunneling, and TAT mechanisms. The metal-insulator-ferroelectric-insulator-metal (MIFIM) structure is considered, with traps located at the TIL-FE interface, forming a continuum trap energy level ( $E_{\text{T}}$ ), and with a trap density ( $N_{\text{T}}$ ) denoting the number of traps per unit interface area. The total current is computed by combining DT/FN tunneling current ( $J_{\text{DT/FN}}$ ) and TAT current ( $J_{\text{TAT}}$ ), expressed as  $J_{\text{total}} = J_{\text{TAT}} + J_{\text{DT/FN}}$ . As shown in Fig. 1(c), the simulation result, which replicates the experimental conditions, shows excellent agreement with that reported by Chu et al.<sup>11</sup> The schematic of the device structure and trap conditions of the simulated FTJ is shown in Fig. 1(d). (For details on the simulation method of the model, including the parameters used to simulate the experimental FTJs, see Sec. S1 of the supplementary material.)

Based on the experimental structure, the 1.5-nm Al<sub>2</sub>O<sub>3</sub>/3-nm HZO/0.6-nm BIL FTJ was initially simu-

<sup>a)</sup>Electronic mail: 281611631kong@gmail.com

<sup>b)</sup>Electronic mail: thhou@nycu.edu.tw

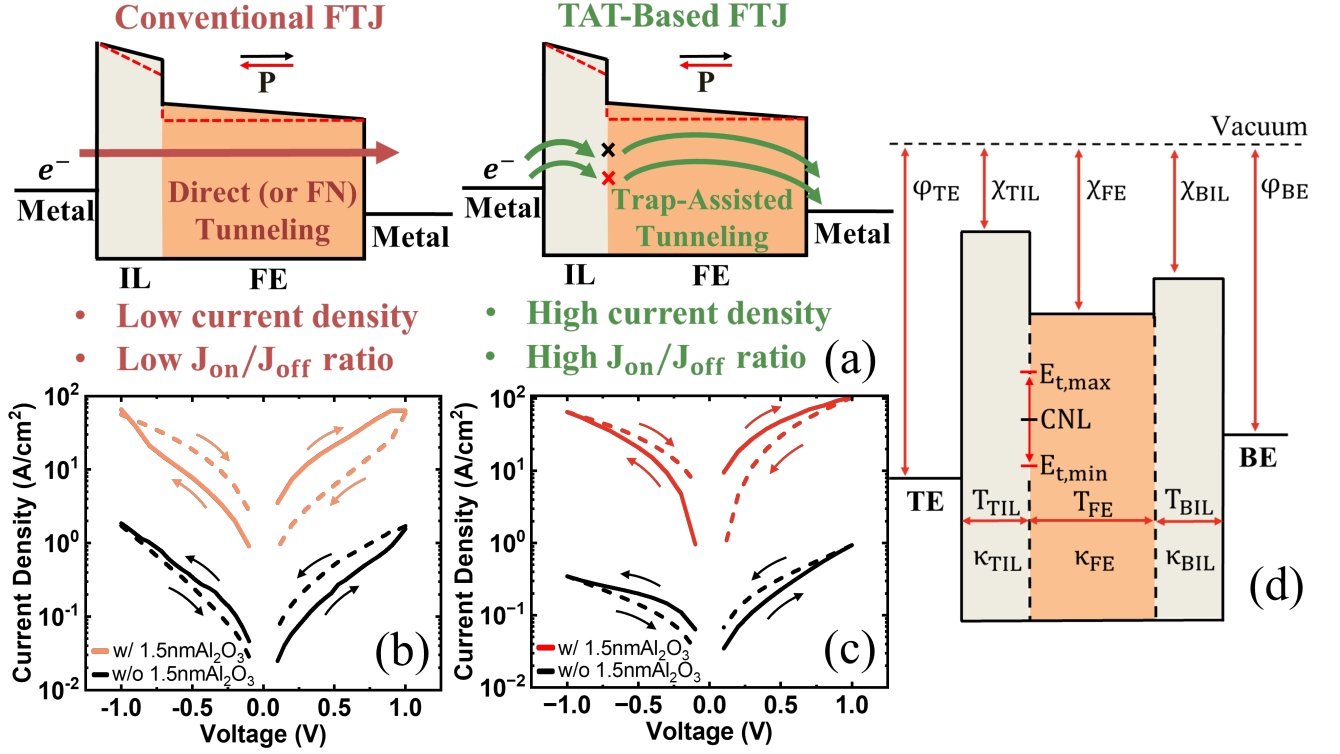


FIG. 1. (a) Comparative schematic of conventional and TAT-based FTJ mechanisms. Conventional FTJ suffers from low  $J_{\text{ON}}$  and low  $J_{\text{ON}}/J_{\text{OFF}}$  ratio, whereas TAT-based FTJ achieves high  $J_{\text{ON}}$  and high  $J_{\text{ON}}/J_{\text{OFF}}$  ratio through appropriate trap modulation. (b) **Reproduced experimental** and (c) **simulated** J-V curves w/ and w/o 1.5 nm Al<sub>2</sub>O<sub>3</sub> in 3 nm HZO FTJ, with sweep voltage  $\pm 1$  V. (d) The schematic of the device structure and trap conditions of the simulated FTJ.

lated. Figure 2 presents the impact of  $E_{\text{T}}$ . The continuum  $E_{\text{T}}$  is assigned at 1.1 eV to 2.9 eV below the FE conduction band ( $E_{\text{CB}}^{\text{FE}}$ ), based on the previous finding<sup>18</sup>, while the metal band offset ( $\varphi_{\text{TE}} - \varphi_{\text{BE}}$ ) is fixed for simplicity. A practical approach to modulating trap behavior involves adjusting the FE band offset ( $\varphi_{\text{BE}} - \chi_{\text{FE}}$ ). As shown in Fig. 2(a), the optimal condition occurs at  $\varphi_{\text{BE}} - \chi_{\text{FE}} = 3$  eV, achieving the best balance between  $J_{\text{ON}}$  and  $J_{\text{ON}}/J_{\text{OFF}}$ . A higher FE band offset significantly reduces  $J_{\text{ON}}$ , while a lower offset rapidly degrades  $J_{\text{ON}}/J_{\text{OFF}}$ .

This performance dependence on continuum  $E_{\text{T}}$  can be explained as the cumulative effect of multiple single-trap scenarios. Figure 2(b) illustrates the dependence of  $J_{\text{TAT}}$  on a single  $E_{\text{T}}$  under positive read voltage. For  $E_{\text{T}} > E_{\text{BE}}$ , the slower BE-to-trap tunneling dominates the BE-to-TE TAT process, causing  $J_{\text{TAT}}$  to increase as  $E_{\text{T}}$  decreases, driven by the exponential increase of carrier injection governed by the Fermi distribution. Conversely, for  $E_{\text{T}} < E_{\text{TE}}$ , trap-to-TE tunneling dominates, and  $J_{\text{TAT}}$  decreases with decreasing  $E_{\text{T}}$  due to the exponential decrease in carrier filling. In the intermediate range ( $E_{\text{BE}} > E_{\text{T}} > E_{\text{TE}}$ ), both BE-to-trap and trap-to-TE tunneling occur from higher to lower energy levels. In this region, carrier injection and filling no longer change exponentially, resulting in a gradual evolution of  $J_{\text{TAT}}$

with  $E_{\text{T}}$ .

The findings in Fig. 2(b) indicate that, in the TAT-based FTJ, the TER effect is governed by distinct  $E_{\text{T}}$  under opposite  $P_{\text{FE}}$  states. Figure 2(c) illustrates the performance dependence on single  $E_{\text{T}}$ , which is set at 2.9 eV below  $E_{\text{CB}}^{\text{FE}}$ .  $J$  under positive  $P_{\text{FE}}$  ( $J_{+\text{P}}$ ) and negative  $P_{\text{FE}}$  ( $J_{-\text{P}}$ ) exhibit similar trends consistent with the previous discussion but offset by  $\Delta E = q\Delta V_{\text{T}}$ , where  $\Delta V_{\text{T}}$  represents the electric potential difference at the TIL-FE interface between two  $P_{\text{FE}}$  states. Notably, the  $J_{\text{ON}}/J_{\text{OFF}}$  ratio exhibits an exponential dependence on  $\Delta E$ , mirroring the trend between  $J_{\text{TAT}}$  and  $E_{\text{T}}$  discussed earlier, and achieves a significantly higher value than that caused by  $J_{\text{DT/FN}}$  alone. However, the  $J_{\text{ON}}/J_{\text{OFF}}$  ratio sharply degrades when  $E_{\text{T}}$  under positive  $P_{\text{FE}}$  ( $E_{\text{T}}^{+\text{P}}$ ) or negative  $P_{\text{FE}}$  ( $E_{\text{T}}^{-\text{P}}$ ) falls within the intermediate range. Therefore, the optimal condition for continuum  $E_{\text{T}}$  under a positive read voltage is achieved when the lowest energy level in the  $E_{\text{T}}^{-\text{P}}$  distribution aligns with  $E_{\text{BE}}$ , ensuring no traps reside in the intermediate range. Similarly, under a negative read voltage, the optimal condition occurs when the lowest energy level in the  $E_{\text{T}}^{+\text{P}}$  distribution aligns with  $E_{\text{TE}}$ .

With optimized  $E_{\text{T}}$ , Fig. 3(a) and 3(b) present the impact of  $N_{\text{T}}$ . As shown in Fig. 3(a), when  $N_{\text{T}}$  is small, DT/FN tunneling dominates, and the device behaves as

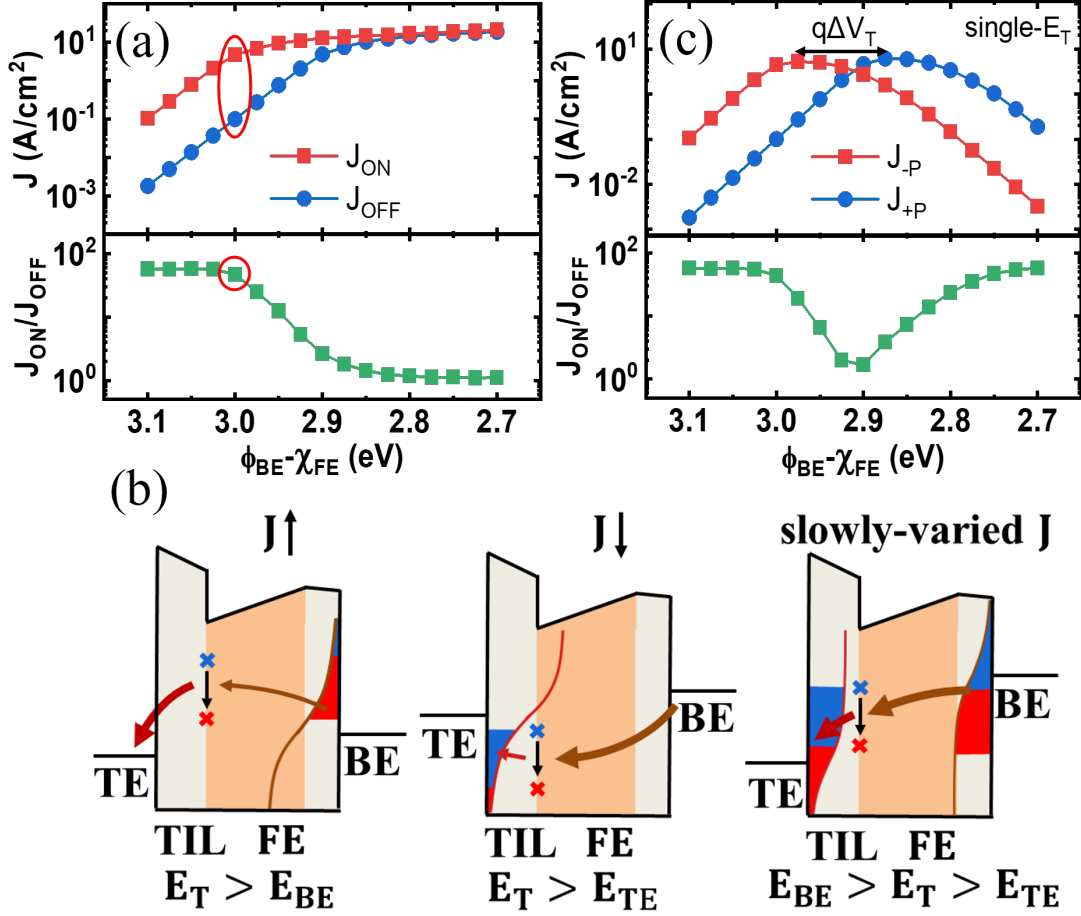


FIG. 2. (a) Continuum-level  $E_T$  dependence of  $J_{TAT}$  under  $V_{write} = 1$  V and  $V_{read} = 0.1$  V. (b) Schematic illustration of the single  $E_T$  dependence of  $J_{TAT}$  under positive  $V_{read}$ . (c) Single  $E_T$  dependence of  $J_{TAT}$  under  $V_{write} = 1$  V and  $V_{read} = 0.1$  V.

a conventional FTJ. As  $N_T$  increases, TAT begins to dominate, leading to higher  $J_{ON}$  without degrading the  $J_{ON}/J_{OFF}$  ratio, as  $J_{TAT}$  is proportional to  $N_T$ .

However, this result holds only when the trap charge ( $Q_T$ ) has limited effects on the local electric potential. Once  $N_T$  exceeds a threshold, the  $J_{ON}/J_{OFF}$  ratio diminishes rapidly. This arises from the Fermi level pinning of the charge neutrality level (CNL), a phenomenon that has been extensively studied in Schottky diodes<sup>19,20</sup>, and has also been extended to dielectric interfaces such as HfO<sub>2</sub>/SiO<sub>2</sub>.<sup>21</sup> CNL is defined as the energy level that must be filled to achieve charge neutrality at the interface and distinguishes between donor-like and acceptor-like traps.<sup>22</sup> When  $CNL > E_F$  (Fermi level at the traps), partially unfilled donor-like traps result in a net positive  $Q_T$ . When  $CNL < E_F$ , partially filled acceptor-like traps result in a net negative  $Q_T$ . As shown in Fig. 3(b), as  $N_T$  increases, CNL in both the on-state ( $CNL_{ON}$ ) and off-state ( $CNL_{OFF}$ ) eventually merges with  $E_F$ , positioned between  $E_{BE}$  and  $E_{TE}$ . At high  $N_T$ , even small energy shifts in CNL produce significant changes in  $Q_T$ , pinning the CNL toward  $E_F$ . As a result, the electric potential

becomes independent of  $P_{FE}$ , resulting in no  $\Delta E$  and suppressing the  $J_{ON}/J_{OFF}$  ratio. The optimal condition at  $N_T = 10^{13}$  cm<sup>-2</sup> preserves a high  $J_{ON}$  while maintaining the  $J_{ON}/J_{OFF}$  ratio. As shown in Fig. 3(c), with the trap condition optimization, despite having identical structural parameters, the TAT-based FTJ demonstrates a significant performance enhancement in both  $J_{ON}$  and  $J_{ON}/J_{OFF}$  compared to the conventional FTJ.

Beyond optimizing trap conditions, structural optimization is also critical to meet the performance demands of IMC. Thickness scaling provides a straightforward strategy to achieve higher  $J_{ON}$ . A FE thickness ( $T_{FE}$ )-dependent  $P_{FE}$  is considered<sup>23</sup> (see Sec. S1 of the supplementary material), while the thickness of unavoidable BIL ( $T_{BIL}$ ) is assumed to remain constant across various  $T_{FE}$  for simplicity due to the identical fabrication process. As shown in Fig. 4(a), the total thickness ( $T_{total}$ ) is scaled down from 5.1 nm to 3.1 nm, maintaining the thickness proportion between the TIL and the FE layer. Under the operation condition of  $V_{write} = 1$  V and  $V_{read} = 0.1$  V, the  $J_{ON}$  of the TAT-based FTJ exceeds 10<sup>3</sup> A/cm<sup>2</sup> at  $T_{total} = 3.1$  nm, while the  $J_{ON}$  of the con-

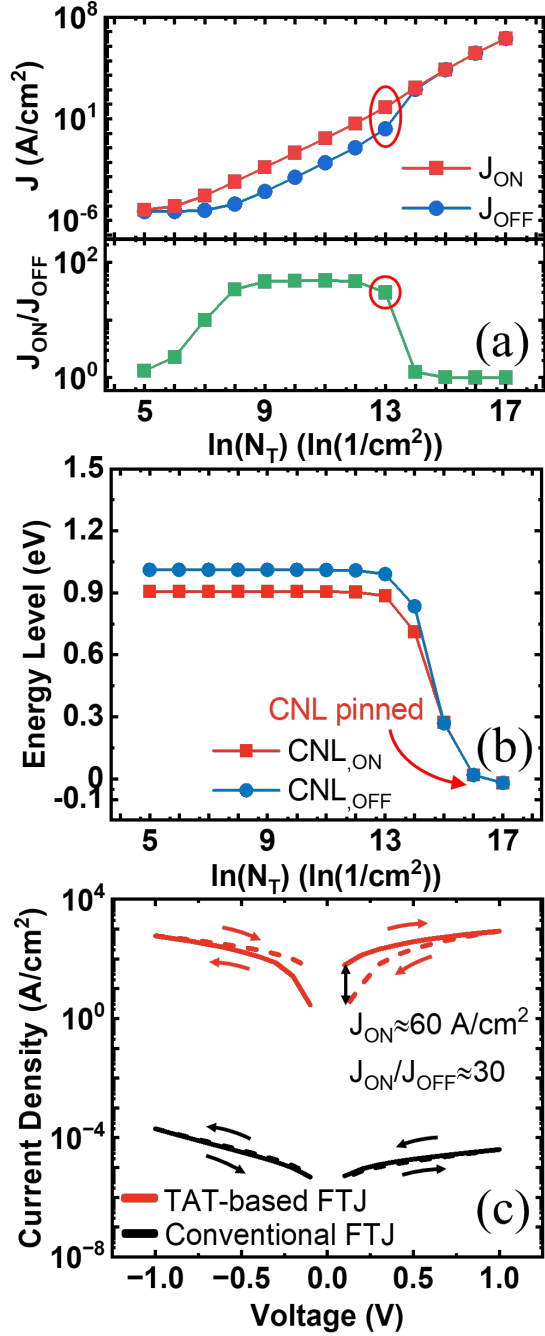


FIG. 3.  $N_T$  dependencies of (a)  $J_{TAT}$  and (b) CNL under  $V_{write} = 1$  V and  $V_{read} = 0.1$  V, with  $E_{BE}$  set to 0 eV and  $E_{TE} = E_{BE} - eV_{read} = -0.1$  eV. (c) J-V curves of the 1.5-nm  $Al_2O_3$ /3-nm HZO/0.6-nm BIL TAT-based FTJ after trap condition optimization and its conventional counterpart under sweep voltage  $\pm 1$  V.

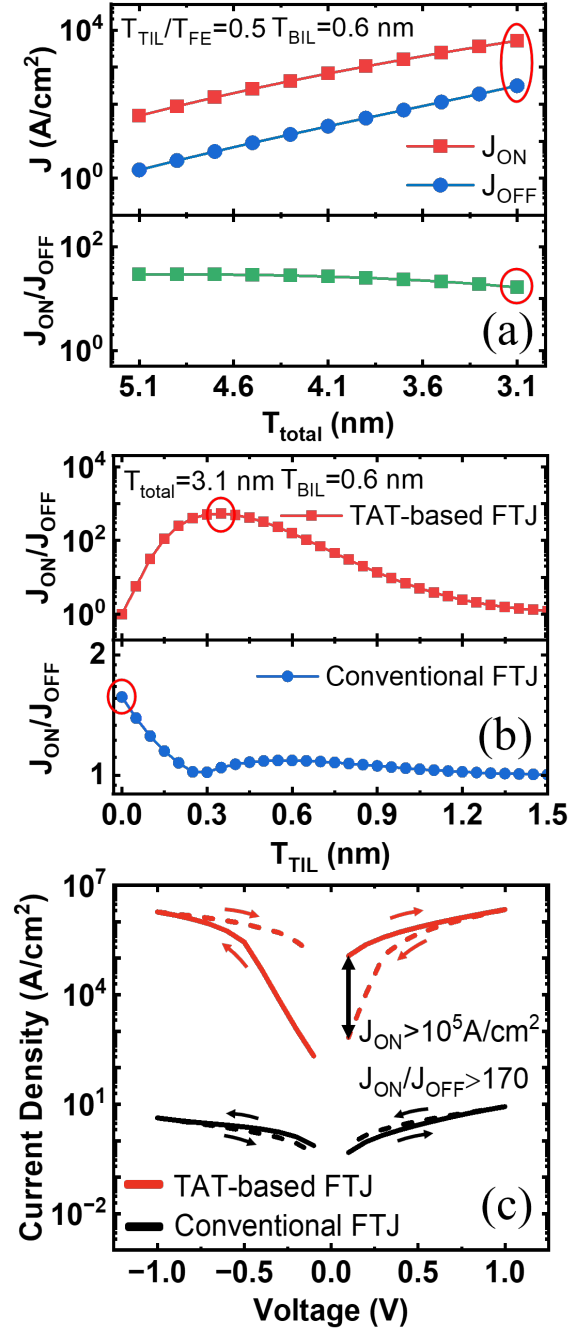


FIG. 4. (a) Thickness scaling of TAT-based FTJ and (b) thickness proportion modulation of TAT-based FTJ and conventional FTJ under  $V_{write} = 1$  V and  $V_{read} = 0.1$  V. (c) J-V curves of the 0.35-nm  $Al_2O_3$ /2.15-nm HZO/0.6-nm BIL TAT-based FTJ and the 2.5-nm HZO/0.6-nm BIL conventional FTJ after device structure optimization under sweep voltage  $\pm 1$  V.

ventional FTJ remains below  $1 \text{ A/cm}^2$  under the same optimization process (see Sec. S2 of the supplementary material). To optimize the  $J_{\text{ON}}/J_{\text{OFF}}$  ratio, the thickness proportion between the TIL and the FE layer is adjusted by varying the TIL thickness ( $T_{\text{TIL}}$ ) while keeping the total thickness constant. Figure 4(b) illustrates the  $J_{\text{ON}}/J_{\text{OFF}}$  ratio of TAT-based and conventional FTJs under different  $T_{\text{TIL}}$  values. Notably, the  $J_{\text{ON}}/J_{\text{OFF}}$  ratio of the TAT-based FTJ is significantly influenced by the trap sites near the TIL due to the oxygen-gathering material used, resulting in a correlation between the  $J_{\text{ON}}/J_{\text{OFF}}$  ratio and  $\Delta V_{\text{T}}$  at the TIL-FE interface. Excessively large  $T_{\text{TIL}}$  causes a substantial voltage drop across the TIL, reducing  $P_{\text{FE}}$  due to its dependence on  $T_{\text{FE}}$  and the minor loop effect.<sup>24,25</sup> Conversely, excessively small  $T_{\text{TIL}}$  induces a large voltage drop across the FE layer, also reducing  $\Delta V_{\text{T}}$ . The optimal  $T_{\text{TIL}}$  occurs at an intermediate value that balances these competing effects, achieving a maximum  $J_{\text{ON}}/J_{\text{OFF}}$  ratio exceeding 500 at  $T_{\text{TIL}} = 0.35 \text{ nm}$  ( $T_{\text{FE}} = 2.15 \text{ nm}$ ). In contrast, the  $J_{\text{ON}}/J_{\text{OFF}}$  ratio of the conventional FTJ primarily depends on the overall energy band variation of the device, where the TIL and BIL exert opposing influences on the switching polarity. The optimal  $T_{\text{TIL}}$  for the conventional FTJ is at  $T_{\text{TIL}} = 0 \text{ nm}$ , as this minimizes the opposing effects of the TIL on the BIL. However, even under the optimal conditions, the  $J_{\text{ON}}/J_{\text{OFF}}$  ratio of the conventional FTJ remains below 2 due to the absence of TAT.

With the optimized device structure, trap condition optimization is revisited to identify the corresponding optimal conditions. The FE band offset of  $\varphi_{\text{BE}} - \chi_{\text{FE}} = 3.1 \text{ eV}$  and the trap density of  $N_{\text{T}} \sim 10^{14} \text{ cm}^{-2}$  are selected to achieve a sufficient  $J_{\text{ON}}$  without compromising the  $J_{\text{ON}}/J_{\text{OFF}}$  ratio of the TAT-based FTJ (see Sec. S3 of the supplementary material). Figure 4(c) compares the optimal performance of the TAT-based FTJ and the conventional FTJ, both with optimized device structures. The TAT-based FTJ achieves  $J_{\text{ON}} > 10^5 \text{ A/cm}^2$  and  $J_{\text{ON}}/J_{\text{OFF}}$  ratio  $> 170$  under low voltage operation, meeting the ultimate requirements for nanoscale IMC.

In conclusion, the characteristics of TAT-based FTJ are comprehensively investigated. Theoretical analysis provides guidelines for optimizing trap conditions and device structure to enhance the  $J_{\text{ON}}$  and  $J_{\text{ON}}/J_{\text{OFF}}$  ratio simultaneously, leveraging the TAT mechanism to overcome the intrinsic bottlenecks of the conventional FTJs. Under optimal conditions, the TAT-based FTJ achieves an ultra-high  $J_{\text{ON}} > 10^5 \text{ A/cm}^2$  and a remarkable  $J_{\text{ON}}/J_{\text{OFF}}$  ratio exceeding 170, significantly outperforming the conventional FTJ and fulfilling the demands of nanoscale IMC. By elucidating these strategies, this study enhances the understanding of TAT-based FTJs and establishes a robust framework for improving their performance, making them strong candidates for IMC applications.

## SUPPLEMENTARY MATERIAL

The supplementary material provides detailed information on the simulation methods of the FTJ model, analysis of conventional FTJ scaling, and trap condition refinement following structural optimization.

## ACKNOWLEDGMENTS

This study is supported by the National Science and Technology Council of Taiwan under grant: 112-2221-E-A49-164-MY3 and 113-2622-8-A49-012-SB.

## AUTHOR DECLARATIONS

### Conflict of Interest

The authors have no conflicts to disclose.

### Author Contributions

**Shi-Xi Kong:** Conceptualization (equal); Data curation (equal); Formal analysis (equal); Investigation (equal); Methodology (equal); Software (equal); Validation (equal); Visualization (equal); Writing – original draft (equal); Writing – review & editing (equal).

## DATA AVAILABILITY

The data that support the findings of this study are available from the corresponding author upon reasonable request.

- <sup>1</sup>U. Schroeder, M. H. Park, T. Mikolajick, and C. S. Hwang, *Nature Reviews Materials* **7**, 653 (2022).
- <sup>2</sup>H.-H. Huang, Y.-H. Chu, T.-Y. Wu, M.-H. Wu, I.-T. Wang, and T.-H. Hou, *IEEE Transactions on Electron Devices* **69**, 4686 (2022).
- <sup>3</sup>T.-Y. Wu, H.-H. Huang, Y.-H. Chu, C.-C. Chang, M.-H. Wu, C.-H. Hsu, C.-T. Wu, M.-C. Wu, W.-W. Wu, T.-S. Chang, H.-Y. Lee, S.-S. Sheu, W.-C. Lo, and T.-H. Hou, in *2019 IEEE International Electron Devices Meeting (IEDM)* (IEEE, 2019) pp. 6–3.
- <sup>4</sup>R. Yang, *Nature Electronics* **3**, 237 (2020).
- <sup>5</sup>J. Yoo, H. Song, H. Lee, S. Lim, S. Kim, K. Heo, and H. Bae, *Electronics* **12**, 2297 (2023).
- <sup>6</sup>S. Yu, H. Jiang, S. Huang, X. Peng, and A. Lu, *IEEE circuits and systems magazine* **21**, 31 (2021).
- <sup>7</sup>W. Haensch, A. Raghunathan, K. Roy, B. Chakrabarti, C. M. Phatak, C. Wang, and S. Guha, *Advanced Materials* **35**, 2204944 (2023).
- <sup>8</sup>H. Ryu, H. Wu, F. Rao, and W. Zhu, *Scientific reports* **9**, 20383 (2019).
- <sup>9</sup>S. S. Cheema, N. Shanker, C.-H. Hsu, A. Datar, J. Bae, D. Kwon, and S. Salahuddin, *Advanced Electronic Materials* **8**, 2100499 (2022).

- <sup>10</sup>N. Siannas, C. Zacharaki, P. Tsipas, S. Chaitoglou, L. Begonlours, and A. Dimoulas, in *ESSDERC 2021 - IEEE 51st European Solid-State Device Research Conference (ESSDERC)* (2021) pp. 287–290.
- <sup>11</sup>Y.-H. Chu, H.-H. Huang, Y.-H. Chen, C.-H. Hsu, P.-J. Tzeng, S.-S. Sheu, W.-C. Lo, C.-I. Wu, and T.-H. Hou, in *2021 International Symposium on VLSI Technology, Systems and Applications (VLSI-TSA)* (IEEE, 2021) pp. 1–2.
- <sup>12</sup>K. Shajil Nair, M. Holzer, C. Dubourdieu, and V. Deshpande, *ACS Applied Electronic Materials* **5**, 1478 (2023).
- <sup>13</sup>J. Yu, T. Wang, Z. Li, Y. Liu, J. Meng, K. Xu, P. Liu, H. Zhu, Q. Sun, D. W. Zhang, and L. Chen, *IEEE Electron Device Letters* **44**, 245 (2022).
- <sup>14</sup>J. Kim, Y. Park, J. Lee, E. Lim, J.-K. Lee, and S. Kim, *Advanced Materials Technologies* **9**, 2400050 (2024).
- <sup>15</sup>Y. Xu, Y. Yang, S. Zhao, T. Gong, P. Jiang, S. Lv, H. Yu, P. Yuan, Z. Dang, Y. Ding, Y. Wang, Y. Chen, Y. Wang, J. Bi, and Q. Luo, *IEEE Transactions on Electron Devices* **69**, 430 (2021).
- <sup>16</sup>X. Guan, S. Yu, and H.-S. P. Wong, *IEEE Transactions on electron devices* **59**, 1172 (2012).
- <sup>17</sup>B. Gao, B. Sun, H. Zhang, L. Liu, X. Liu, R. Han, J. Kang, and B. Yu, *IEEE Electron Device Letters* **30**, 1326 (2009).
- <sup>18</sup>Y. L. Zhang, Y. Shao, X. Lu, M. Zeng, Z. Zhang, X. Gao, X. Zhang, J. Liu, and J. Dai, *Applied Physics Letters* **105** (2014).
- <sup>19</sup>N. Newman, W. E. Spicer, T. Kendelewicz, and I. Lindau, *Journal of Vacuum Science & Technology B: Microelectronics Processing and Phenomena* **4**, 931 (1986).
- <sup>20</sup>F. Léonard and J. Tersoff, *Physical Review Letters* **84**, 4693 (2000).
- <sup>21</sup>X. L. Wang, W. Wang, K. Han, J. Zhang, J. Xiang, X. Ma, H. Yang, D. Chen, and T. Ye, *ECS Transactions* **45**, 119 (2012).
- <sup>22</sup>J. Lyu, I. Fina, R. Solanas, J. Fontcuberta, and F. Sánchez, *ACS Applied Electronic Materials* **1**, 220 (2019).
- <sup>23</sup>A. M. Cowley and S. M. Sze, *Journal of Applied Physics* **36**, 3212 (1965).
- <sup>24</sup>K. Ni, M. Jerry, J. A. Smith, and S. Datta, in *2018 IEEE symposium on VLSI technology* (IEEE, 2018) pp. 131–132.
- <sup>25</sup>S. L. Miller, R. D. Nasby, J. Schwank, M. S. Rodgers, and P. V. Dressendorfer, *Journal of Applied Physics* **68**, 6463 (1990).